Synthesis, Nuclear, and Magnetic Structures and Magnetic Properties of $[Mn_3(OH)_2(SO_4)_2(H_2O)_2]$

Mohsen Ben Salah,[a, b] Serge Vilminot,*[a] Gilles André,[c] Mireille Richard-Plouet,[a, d] Françoise Bourée-Vigneron,[c] Tahar Mhiri,[b] and Mohamedally Kurmoo[a]

Abstract: $[Mn_3(OH)_2(SO_4)_2(H_2O)_2]$ and its deuterated anlaogue were synthesized by a hydrothermal technique and characterized by differential thermal analysis, thermogravimetric analysis, and IR spectroscopy. Its nuclear structure, determined by single-crystal X-ray analysis and Rietveld analysis of neutron powder-diffraction data, consists of a 3D network of chains of edge-sharing $Mn(1)O_6$, running along the *c* axis, connected by the apices of $Mn(2)O_6$ and SO_4 units. It is isostructural to the nickel analogue. Determination of the magnetic structure and measurements of magnetization and heat capacity indicate the coexistence of both magnetic long-range ordering (LRO) and short-range ordering (SRO) below a Néel temperature of 26 K, while the SRO is retained at higher temperatures. The moments of the two independent Mn atoms lie in the *bc* plane, and that of Mn(1) rotates continuously by 54° towards the *c* axis on decreasing the temperature from 25 to 1.4 K. While the SRO may be associated with frustration of the moments within a Mn_3 trimer, the LRO is achieved by antiparallel alignment of the four symmetry-related trimers within the magnetic unit cell. A spin-flop field, measured by dc and ac magnetization on a SQUID, is observed at 15 kOe.

Keywords: hydrothermal synthesis · hydroxide sulfates · magnetic properties · manganese

Introduction

Recently, there has been widespread interest in hydrothermal synthesis from the viewpoints of a) producing high-purity crystalline solids which are either known in nature or are unknown,[1,2] b) recrystallizing fairly insoluble framework or layered compounds,[3] c) designing coordination polymers,[4,5] and d) most importantly in creating porous compounds.[6] These interests, among others, are driven by 1) the need to fully characterize minerals for understanding certain geological hypotheses,[7] 2) the existence of unusual collective properties, such as electrical conductivity, magnetism and optical behavior,[8] and 3) applications in catalysis, selective separation, and gas storage in the case of porous materials.[9] Our current interest is in the characterization of new solids with potential magnetic properties, and in the past few years, we have investigated mineral-like compounds of the iron group metals. Following our studies on magnetic phyllosilicates[10] that contain μ_3-OH groups and a SiO_n network favoring a layered structure, we have now replaced the silicate by sulfate, which in principle should favor both 2D and 3D structures.[11,12] The reasons for this choice were that μ_3-OH can be used to bring moment-bearing transition-metal atoms closer together and thus lead to more efficient magnetic exchange, while the sulfate ion can exhibit terminal or bridging μ_2, μ_3, or μ_4 bonding modes and generate close-packed structures. While OH can be considered as a single-atom connector, a bridging sulfate group is a three-atom connector.

Using the above approach, we have obtained and characterized a set of isostructural framework compounds $[M_3(OH)_2(SO_4)_2(H_2O)_2]$ (M = Ni, Co, Mn). In a previous

[a] Dr. M. Ben Salah, Dr. S. Vilminot, Dr. M. Richard-Plouet, Dr. M. Kurmoo
Groupe des Matériaux Inorganiques
IPCMS, UMR 7504 CNRS-ULP
23 rue du Loess, BP 43
67034 Strasbourg Cedex 2 (France)
E-mail: vilminot@ipcms.u-strasbg.fr

[b] Dr. M. Ben Salah, Prof. Dr. T. Mhiri
Laboratoire de L'Etat Solide
Faculté des Sciences
3038 Sfax (Tunisia)

[c] Dr. G. André, Dr. F. Bourée-Vigneron
Laboratoire Léon Brillouin
CEA-CNRS, CEA Saclay
91191 Gif-sur-Yvette Cedex (France)

[d] Dr. M. Richard-Plouet
Institut des Matériaux Jean Rouxel, UMR CNRS 6502
Laboratoire de Chimie des Solides
2 rue de la Houssinière, BP 32229,
44322 Nantes Cedex 03 (France)

Supporting information for this article is available on the WWW under http://www.chemeurj.org/ or from the author.

DOI: 10.1002/chem.200305645

paper,[12a] we presented the nuclear and magnetic structures and the magnetic properties of $[Ni_3(OH)_2(SO_4)_2(H_2O)_2]$. The nuclear structure consists of corrugated planes of nickel octahedra connected to each other through sulfate groups. The magnetic properties are characterized by a transition from a paramagnetic to a canted antiferromagnetic ordered state at 29 K. Accordingly, the magnetic structure from neutron powder-diffraction data revealed an antiparallel arrangement of the moments of Ni(1) and Ni(2) within a trimer unit [two symmetry related Ni(1) and one Ni(2)] and antiparallel arrangement of the symmetry-related trimers in the unit cell. The magnetic moments of both kinds of Ni^{2+} are aligned along the *b* axis. Given the difference in ionic radii, spin quantum numbers and single-ion anisotropies of the transition metals it was judicious to synthesize the cobalt and manganese analogues, and here we present the synthesis of the manganese compound, which is more complex than for nickel, its X-ray single-crystal nuclear structure at 295 K, its crystal structure from neutron data at several temperatures between 1.4 and 300 K and the associated magnetic structure at low temperature. Interestingly, magnetic and heat-capacity measurements and neutron diffraction data reveal the presence of a persistent short-range order in addition to a long-range antiferromagnetic ordering below 26 K. Two other minor phases were occasionally observed. One of them, $[Mn_2(OH)_2SO_4]$, which has the habit of pink prismatic blocks, was identified by single-crystal X-ray diffraction. The other, which forms fine colourless needles, has not been structurally characterized, though X-ray powder diffraction (XRPD) indicates a possible layered structure with an interlayer distance of 9.67 Å. A full paper on the structural and magnetic characteristics of the cobalt analogue is in preparation.

Abstract in French: *$[Mn_3(OH)_2(SO_4)_2(H_2O)_2]$ et son équivalent deutérié ont été préparés par synthèse hydrothermale et caractérisés par ATG-ATD et spectroscopie infrarouge. Sa structure, affinée à partir de données de diffraction RX sur monocristal, est analogue à celle du sel de nickel correspondant et fait apparaître un réseau 3D formé par des chaînes d'octaèdres $Mn(1)O_6$ liés par une arête, chaînes connectées entre elles par un sommet commun à des octaèdres $Mn(2)O_6$ et des tétraèdres SO_4. La détermination de la structure magnétique et les mesures des propriétés magnétiques et de chaleur spécifique indiquent la coexistence d'un ordre magnétique à longue distance (LRO) et à courte distance (SRO) endessous de la température de Néel T_N de 26 K, l'ordre à courte distance s'établissant à plus haute température. Les moments magnétiques des deux atomes Mn indépendants se trouvent dans le plan bc. Alors que celui de Mn(2) est toujours dirigé selon l'axe c, celui de Mn(1) se rapproche progressivement de cette direction lorsque la température est abaissée de T_N à 1,4 K, la rotation globale étant de 54°. Alors que l'ordre à courte distance peut être dû à la frustation des moments à l'intérieur des trimères Mn_3, en interaction antiferromagnétique, l'ordre à longue distance résulte de l'alignement antiparallèle des quatre trimères de la maille magnétique. Un champ de spin-flop, mesuré par aimantation dc et ac, est observé à 15 kOe.*

Results and Discussion

Synthesis: Under the conditions of hydrothermal synthesis used for nickel, manganese(II) yields Mn_2O_3 and MnO as brown to black solids as the main phases. This result is related to the low stability of Mn^{2+} in basic aqueous solution and its relative ease of oxidation to Mn^{3+} and Mn^{4+}.[13] To avoid or at least to restrict oxidation to higher valence manganese, experiments were performed in freshly boiled distilled water to eliminate soluble gases. This results in a very small amount of dark materials whose presence is not evidenced by X-ray diffraction within the detection limits, possibly due to their small size and amorphous nature. Furthermore, saturating the boiled water with argon resulted in no noticeable improvement. However, shortening the time between mixing the reactants and sealing the reactor reduces the amount of black oxide products considerably. Finally, to be certain that measurements were made on a single phase, samples were examined and cleaned from the other two phases under an optical microscope. Interestingly, the concentration of reactants and reaction temperature have less effect on manganese oxidation, though we find that shorter reaction times than were used in the preparation of the nickel analogue result in higher quality and purer compounds.

Powder X-ray diffraction studies: The X-ray powder diffraction pattern (Figure S1, Supporting Information) is analogous to that of $[Ni_3(OH)_2(SO_4)_2(H_2O)_2]$. Indeed, the same sequence of diffraction peaks is observed but with a noticeable shift of the corresponding peaks towards lower angles. This shift logically follows from the larger ionic radius of manganese (Ni^{2+} 0.74 Å, Mn^{2+} 0.95 Å), which results in an increase of the average M–O distance from 2.068 for Ni to 2.183 Å for Mn.[12a,14] Therefore, it was possible to use the U-FIT program[15] to index most of the diffraction peaks and to refine the unit-cell parameters. This confirmed that the Mn compound is isostructural to the Ni analogue. The powder-diffraction peaks indexed as (100), (200), and (300) are very intense compared to all the others, and suggest preferential orientation in the Bragg–Brentano geometry used. In addition, we note in some cases the presence of only one of the minor impurities, identified by a diffraction peak corresponding to $d = 9.67$ Å.

Thermal analysis: The TGA trace recorded in air at a heating rate of $3\,^{\circ}C\,min^{-1}$ shows four successive weight-losses (Figure S2, Supporting Information). The first, centered at 300 °C, and the second, at 400 °C, are attributed to dehydration. The first can be associated with the removal of coordinated water molecules and the second to the hydroxyl groups, with a 3/1 ratio. However, a 2/1 ratio would be expected according to the chemical formula $[Mn_3(OH)_2(SO_4)_2(H_2O)_2]$. The difference was attributed to rapid oxidation of the resulting MnO to Mn_2O_3 accompanying the loss

of the OH group. The X-ray diffraction pattern recorded on a sample heated to 500 °C at the same heating rate only reveals the presence of β-$MnSO_4$. The third weight loss, at 770 °C, is attributed to the decomposition of β-$MnSO_4$ yielding, according to X-ray diffraction, Mn_2O_3. The fourth, at about 900 °C, is related to reduction of Mn_2O_3 to Mn_3O_4, as revealed by X-ray diffraction. All weight losses are associated with endothermic effects on the corresponding differential thermal analysis (DTA) trace. However, while the first and last peaks are clearly endothermic, the second and third ones result from a combination of heat consumption due to losses of H_2O and SO_3 and of heat generation owing to oxidation of MnO, which results in broadening of the second peak and a jump for the third peak. These results allowed us to propose a decomposition scheme for $[Mn_3(OH)_2(SO_4)_2(H_2O)_2]$ (Table 1).

Table 1. Decomposition scheme for $[Mn_3(OH)_2(SO_4)_2(H_2O)_2]$.

Temperature [°C]	Chemical reaction	Calculated weight loss [%]	Observed weight loss [%]
300	$[Mn_3(OH)_2(SO_4)_2(H_2O)_2] \rightarrow Mn_3(OH)_2(SO_4)_2 + 2H_2O$	8.4	8.7
400	$[Mn_3(OH)_2(SO_4)_2] \rightarrow 2MnSO_4 + MnO + H_2O$		
	$MnO + 1/2\,O_2 \rightarrow 1/2\,Mn_2O_3$	2.3	2.7
770	$1/2\,Mn_2O_3 + 2MnSO_4 \rightarrow 1/2\,Mn_2O_3 + 2MnO + 2SO_3$		
	$2MnO + 1/2\,O_2 \rightarrow Mn_2O_3$	33.7	33.4
910	$3/2\,Mn_2O_3 \rightarrow Mn_3O_4 + 1/4\,O_2$	1.9	1.9

The presence of minor secondary phases, sometimes revealed by X-ray diffraction, is another source for the discrepancies between theoretical and observed weight losses. From the residual mass, the estimated manganese content of the compound is 38.4 % (theoretical value 38.6 %).

Single-crystal X-ray structure: The structure of $[Mn_3(OH)_2(SO_4)_2(H_2O)_2]$ (Tables 2 and 3) is strictly the same as that of the corresponding nickel compound.[12a] Therefore, a short description will suffice here. The three-dimensional network is built up of the coordination polyhedra around manganese (octahedron) and sulfur (tetrahedron). Chains of edge-sharing octahedra around Mn(1) ions along the *c* axis are connected to each other by means of corner-sharing Mn(2) octahedra to give corrugated sheets parallel to the *bc* plane (Figure 1). The sulfate tetrahedra make the connections between the corrugated sheets and between the Mn(2) octahedra. The Mn(1) chains consist of dimers alternately rotated by 180° (see Figure 9 below), giving rise to zigzag chains. The octahedron around Mn(1) is slightly more distorted than that around Mn(2) (Table 4), whereas both sulfate tetrahedra are nearly regular. While the deviation of the M–O bond lengths of the Mn compound from normal values are of the same order as for the Ni compound, the distortions of the angles within the MO_6 octahedra are more severe, with values as high as 111° instead of 90° or as low as 162° instead of 180°.

The oxygen atoms are of three kinds according to their environments:

Table 2. Summary of the single-crystal X-ray data collection at 295 K and structure refinement of $[Mn_3(OH)_2(SO_4)_2(H_2O)_2]$.

a [Å]	7.2852(2)	*hkl* range	$-9<h<9$, $-13<k<14$, $-18<l<18$
b [Å]	9.9568(3)	θ range	3.07–29.98
c [Å]	13.2519(5)	total reflections	2454
V [Å^3]	961.26(5)	unique reflections	1390
Z	4	unique reflections with $\lvert I_o\rvert > 2\sigma(I_o)$	1211
space group	*Pbcm* (no. 57)	R_{int} [%]	2.69
F (000)	812	R_F (all data)[a] [%]	4.16
ρ_{calcd} [g cm^{-3}]	2.950	$wR(F_o^2)$[b] (all data) [%]	9.44
μ [mm^{-1}]	4.235	GoF [%]	1.094

[a] $R_F = \Sigma\,||F_o| - |F_c||/\Sigma\,|F_o|$. [b] $wR = \{\Sigma[w(F_o^2 - F_c^2)^2]/\Sigma[w(F_o^2)^2]\}^{1/2}$, $w = 1/[\sigma^2(F_o^2) + (0.0503\,P)^2 + 1.4540\,P]$, where $P = (F_o^2 + 2F_c^2)/3$

Table 3. Fractional atomic coordinates for $[Mn_3(OH)_2(SO_4)_2(H_2O)_2]$ obtained from X-ray data at 295 K.

Atom	*x*/*a*	*y*/*b*	*z*/*c*
Mn(1)	0.06402(6)	0.03169(4)	0.12842(3)
Mn(2)	0.29954(8)	0.74040(6)	0.25
S(1)	0.79273(12)	0.25	0
S(2)	0.29971(12)	0.41416(9)	0.25
O(1)	0.5831(4)	0.0344(3)	0.25
O(2)	0.0874(3)	0.6289(2)	−0.0035(2)
O(3)	0.3248(3)	0.7454(2)	0.0893(2)
O(4)	0.4111(4)	0.2921(3)	0.25
O(5)	0.1815(3)	0.4144(2)	0.1590(2)
OH(1)	0.7846(4)	0.4463(3)	0.25
OH(2)	0.0253(4)	0.6639(3)	0.25
OW	0.3058(3)	0.1117(2)	0.0536(2)
H(1)[a]	0.7200	0.4947	0.25
H(2)[a]	0.0644	0.2401	0.25
HW(1)[a]	0.3841	0.1807	0.0690
HW(2)[a]	0.3238	0.3756	0.4784

[a] Coordinates from difference Fourier maps not refined for the H atoms.

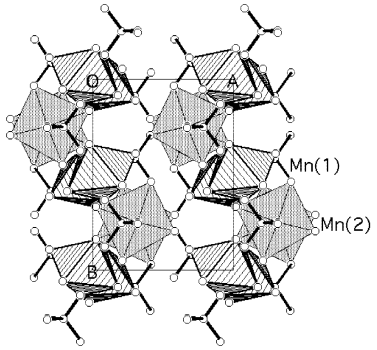

Figure 1. Projection of the crystal structure along the *c* axis. Mn(1) in striped octahedra, Mn(2) in gray octahedra and sulfate as balls and sticks.

Table 4. Interatomic distances [Å] and angles [°] from X-ray structure determination and those involving the D atoms from neutron powder data at 300 K.

S(1)–O(3)	1.461(2)×2	O(3)-S(1)-O(3)	108.3(2)	O(2)-S(1)-O(2)	108.2(2)
S(1)–O(2)	1.489(2)×2	O(3)-S(1)-O(2)	110.05(11)×2	⟨O-S(1)-O⟩	109.5
⟨S–O⟩	1.475	O(3)-S(1)-O(2)	110.11(11)×2		
S(2)–O(4)	1.461(3)	O(4)-S(2)-O(1)	110.8(2)	⟨O-S(2)-O⟩	109.5
S(2)–O(1)	1.470(3)	O(4)-S(2)-O(5)	108.90(11)×2		
S(2)–O(5)	1.482(2)×2	O(1)-S(2)-O(5)	109.66(11)×2		
⟨S–O⟩	1.474	O(5)-S(2)-O(5)	108.9(2)		
Mn(1)–OH(1)	2.130(2)	OH(1)-Mn(1)-OW	94.12(9)	OW-Mn(1)-O(2)	82.36(8)
Mn(1)-OW	2.173(2)	OH(1)-Mn(1)-O(5)	94.03(10)	O(5)-Mn(1)-OH(2)	86.63(9)
Mn(1)–O(5)	2.174(2)	OH(1)-Mn(1)-OH(2)	80.60(8)	O(5)-Mn(1)-O(2)	88.45(8)
Mn(1)–OH(2)	2.180(2)	OH(1)-Mn(1)-O(2)	177.52(9)	O(5)-Mn(1)-O(2)	79.76(8)
Mn(1)-O(2)	2.282(2)	OH(1)-Mn(1)-O(2)	103.16(8)	OH(2)-Mn(1)-O(2)	99.53(8)
Mn(1)–O(2)	2.308(2)	OW-Mn(1)-O(5)	161.62(9)	OH(2)-Mn(1)-O(2)	166.07(9)
⟨Mn1–O⟩	2.208	OW-Mn(1)-OH(2)	110.95(10)	O(2)-Mn(1)-O(2)	77.30(8)
		OW-Mn(1)-O(2)	83.51(8)		
Mn(2)–OH(2)	2.138(3)	OH(2)-Mn(2)-O(3)	95.08(5)×2	O(3)-Mn(2)-O(4)	84.89(5)×2
Mn(2)–O(3)	2.138(2)×2	OH(2)-Mn(2)-OH(1)	94.21(10)	O(3)-Mn(2)-O(1)	89.33(6)×2
Mn(2)–OH(1)	2.139(3)	OH(2)-Mn(2)-O(4)	172.88(11)	OH(1)-Mn(2)-O(4)	92.92(10)
Mn(2)–O(4)	2.170(3)	OH(2)-Mn(2)-O(1)	91.76(10)	OH(1)-Mn(2)-O(1)	174.03(10)
Mn(2)–O(1)	2.223(3)	O(3)-Mn(2)-O(3)	169.78(11)	O(4)-Mn(2)-O(1)	81.12(11)
⟨Mn2–O⟩	2.158	O(3)-Mn(2)-OH(1)	90.15(6)×2		
Mn(1)···Mn(1)	3.223(2)	Mn(1)-OH(1)-Mn(1)	98.3(1)	Mn(1)-O(2)-Mn(1)	102.7(1)
Mn(1)···Mn(1)	3.585(2)	Mn(1)-OH(2)-Mn(1)	95.3(1)	Mn(1)-OH(1)-Mn(2)	122.1(2)
				Mn(1)-OH(2)-Mn(2)	116.6(2)
OD(1)–D(1)	0.946(10)	D(1)···O(1)	1.865(10)	OD(1)-D(1)···O(1)	169(9)
OD(2)–D(2)	0.937(13)	D(2)···O(5)	2.339(10)×2	OD(2)-D(2)···O(5)	147(3)
OW–DW(1)	0.923(10)	DW(1)···O(3)	2.203(9)	OW-DW(1)···O(3)	161(4)
OW–DW(2)	0.914(11)	DW(2)···O(5)	2.157(10)	OW-DW(2)···O(5)	151(3)
DW(1)···DW(2)	1.454(10)			DW(1)-OW-DW(2)	105(2)

1) The oxygen atoms of the water molecules are terminally bonded to Mn(1).
2) The oxygen atoms O(1), O(3), O(4), and O(5) are of the μ_2-oxo type and bonded to S and Mn(1) or Mn(2); the Mn-O-S angles are in the range 120–140°, in accordance with repulsion between bonding pairs.
3) The oxygen atoms of the hydroxyl groups and oxygen atom O(2) are bonded to three atoms, either Mn only [OH(1) and OH(2)] or two Mn and one S [O(2)]; they can be classified as μ_3-hydroxo [OH(1) and OH(2)] and μ_3-oxo [O(2)].

The thermal parameters of the oxygen atom OW of the water molecule are much higher than those of the other oxygen atoms; the U_{eq} value of 200×10^{-4} Å^2 for OW compares to mean values of 90×10^{-4} and 125×10^{-4} Å^2 for OH and sulfate O atoms, respectively. Furthermore, careful inspection of the Fourier maps does not reveal any splitting of the OW atom.

The structure refined from neutron powder-diffraction data (Table 5 and Table S2, Supporting Information) is in good agreement with the single-crystal X-ray structure, even for the positions of the sulfur atoms, which in the case of the Ni analogue result in strong distortions of the sulfate tetrahedra.[12a] It appears that data collection with the G4.2 apparatus (this work) is more suitable for our compounds than the 3T2 apparatus used for the Ni compound. The refinement also confirms that deuteration was achieved at a high level with a D/(D+H) ratio of 0.91. The D atoms are involved in weak deuterium bonds (Table 4), the shortest D···O distance being 1.865 Å. While D(1), DW(1), and DW(2) define single deuterium bonds, D(2) is shared between two oxygen atoms, which results in a smaller O–D···O angle. In the heavy water molecule the O–D distances are nearly the same, and the D-O-D angle is 105°. As in the case of the X-ray refinement, the thermal parameter of the oxygen atom of the water molecule ($B=1.64$ Å^2) is higher than those of the others ($B=0.52$ and 1.36 Å^2 for OD and oxygen atoms of sulfate groups, respectively) and the same is true for the related deuterium atoms. This has been attributed to the fact that the water molecule is terminally bound. Therefore, it has more degrees of freedom than the other

Table 5. Crystallographic data and refinement characteristics from neutron powder data for the deuterated compound at 300 K and 1.4 K

	300 K	1.4 K
system	orthorhombic	orthorhombic
space group	*Pbcm* (no. 57)	*Pbcm* (no. 57)
a [Å]	7.30594(9)	7.2953(3)
b [Å]	9.9685(1)	9.9533(3)
c [Å]	13.2738(1)	13.2672(5)
λ [Å]	2.3433	2.4266
2θ range and step	3–171.9°/0.1°	9–88.9°/0.1°
reflections (nuclear)	335	106
reflections (magnetic)	–	386
number of parameters	53	56
R_p [%]	11.1	10.1
R_{wp} [%]	10.8	10.7
R_{exp} [%]	4.21	2.01
R_B [%]	7.26	3.94
R_F [%]	4.99	2.76
GoF [%]	6.57	
$R_{magneticLRO}$ [%]		5.99
$R_{magneticSRO}$ [%]		13.6

oxygen atoms, which are bonded to two or three atoms (S and/or Mn). The observed and calculated neutron powder-diffraction patterns can be found in the Supporting Information (Figure S3).

Infrared spectroscopy: The IR spectra of $[Mn_3(OH)_2(SO_4)_2(H_2O)_2]$ and $[Mn_3(OD)_2(SO_4)_2(D_2O)_2]$ are given in the Supporting Information (Figure S4); the latter is the sample used for neutron powder diffraction with a D/(D+H) ratio of 0.91, as determined by structure refinement. Comparison of the two spectra allows one to distinguish between vibrational bands related to OH and H_2O groups, which shift on deuteration, and those belonging to the SO_4 groups, which do not. Therefore, bands between 3550 and 3400 cm^{-1}, and at about 1600 cm^{-1} and about 870 cm^{-1} can be attributed to the former groups, as they decrease in energy by the expected factor of $(1/2)^{1/2}$ on replacing H by D, whereas the bands between 1200 and 990 cm^{-1} and between 650 and 600 cm^{-1} can be assigned to the latter, as they are not affected by deuteration.

The vibrational bands in the region 3600–3400 cm^{-1} can be attributed to the valence stretching modes of the O–H bonds of OH groups and water molecules. The observation of sharp bands indicates that such groups are involved in weak or very weak hydrogen bonds. According to the neutron powder-diffraction data (Table 4), the shortest D···O distance is 1.865 Å between D(1) and O(1), that is, a weak hydrogen bond. All other distances are longer than 2.15 Å and it can therefore be concluded that D(2), DW(1), and DW(2) are involved in very weak hydrogen bonds. For the H sample (Figure S4, Supporting Information), two bands clearly appear at 3548 and 3396 cm^{-1} in addition to a shoulder at 3466 cm^{-1}. For the D sample (Figure S4), three bands and one shoulder are observed around 2550 cm^{-1}, while the intensities of the bands in the region 3550–3400 cm^{-1} are strongly reduced in accordance with the high D content of the sample. For the D sample, a tentative assignment of the O–D stretching bands is proposed (Table 6)

Table 6. Tentative assignments of ν_{OD} frequencies according to interatomic distances and bond valence calculations.

ν_{OD} [cm^{-1}]	D	D···O [Å]	O	Σs[a]	H/D ratio
2515	D(1)	1.865	O(1)	0.079	0.15/3.85
2544	D(2)	2.34×2	O(5)×2	0.044	0.31/3.69
2624	DW(2)	2.157	O(5)	0.035	1.14/6.86
2645	DW(1)	2.203	O(3)	0.032	0.59/7.41

[a] $s=\exp[(r_0-r)/B]$, where s = bond valence, $r_0=0.882$ (H) or 0.927 (D), $B=0.37$. $\Sigma s=[n_H/(n_H+n_D)]s(H)+[n_D/(n_H+n_D)]s(D)$

on the basis of ν_{OD} versus interatomic O···O distance correlation diagrams.[16] In our case, as the D···O distances are known, the discussion concerns these data. The shortest D···O distance (i.e., D(1)···O(1) 1.865 Å) can be unambiguously assigned to the band at 2515 cm^{-1}. The other three bands appear at 2544, 2624 and 2645 cm^{-1} with relative intensities of 1:2:2. Consideration of the D···O distances relates them to DW(2), DW(1), and D(2), respectively. This result disagrees with the expected intensities of 2:2:1 for their numbers in the unit cell. Therefore, we calculated bond valences according to the model of Brown and Altermatt.[17] From the resulting data (Table 6), it appears that the bond valences of the DW atoms are similar, and we can then assign the bands at 2624 and 2645 cm^{-1} to DW···O deuterium bonds. The bending mode of water molecules is expected to be at about 1600 cm^{-1}. However, two bands at 1623 and 1602 cm^{-1} are always observed. The latter was attributed to the presence of some second phase, since its intensity strongly decreased when rectangular platelet crystals of $[Mn_3(OH)_2(SO_4)_2(H_2O)_2]$ were selected. For the D sample, the band at about 1600 cm^{-1} nearly disappeared, in agreement with the 91 % D content. The low-energy bands related to OH groups and H_2O appear at 917, 835 and 797 cm^{-1}, and they lie outside of the measuring range for the D sample. They were attributed to libration modes. The remaining bands in the spectra are vibration modes of sulfate groups: ν_3 and ν_4 at about 1100 and 600 cm^{-1}, respectively. Considering the local symmetry of the SO_4 tetrahedra, one observes a lowering compared to the T_d regular symmetry in accordance with different S–O bond lengths and different environment of the oxygen atoms due to Mn ions. These distortions explain the presence of numerous bands around 1100 cm^{-1}, whereas the band at 995 cm^{-1} can be attributed to the symmetric stretching ν_1 vibration mode that becomes IR-active by lowering of symmetry.

Magnetic susceptibility studies: In the paramagnetic region, the magnetic susceptibility of a randomly oriented sample follows the Curie–Weiss law $\chi=C/(T-\theta)=14.16/(T+75)$ emu mol^{-1}, where the Curie and Weiss constants were obtained by fitting the experimental $1/\chi$ data in the temperature range 100–300 K (Figure 2). The negative θ

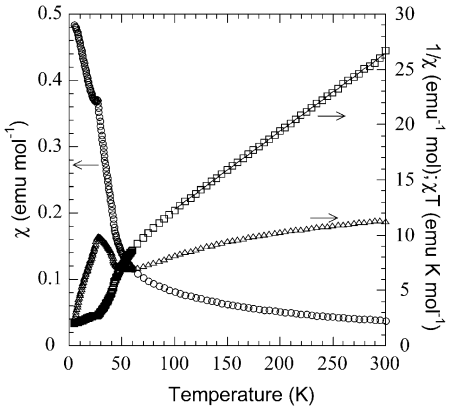

Figure 2. Temperature dependence of the dc susceptibility (circles), reciprocal dc susceptibility (squares) and the product of susceptibility and temperature (triangles). The solid line is the fit to the Curie–Weiss function for data above 100 K.

value, exemplified by the decrease in the χT product, suggests the dominance of antiferromagnetic exchange interactions. From the Curie constant ($C=Ng^2\mu_B^2 s(s+1)/3k$) of 4.72 emu K per Mn atom and $s=5/2$, we deduce a value of the Landé g factor of 2.07. With decreasing temperature, χT exhibits a minimum at 40 K before reaching a sharp maxi-

mum at 26 K. This behavior is characteristic of a ferrimagnet.[18] However, the transition at 26 K is not associated with long-range ferrimagnetic ordering, due to the absence of spontaneous magnetization in a small applied field, but is assigned to the Néel temperature T_N of the long-range antiferromagnetic ordering, as confirmed by the λ-type anomaly in the specific heat. At lower temperature an unusual gradual increase in susceptibility is observed. In addition, the real part of the ac susceptibility exhibits a peak at 26 K, and there is no anomaly in the imaginary component (Figure 3),

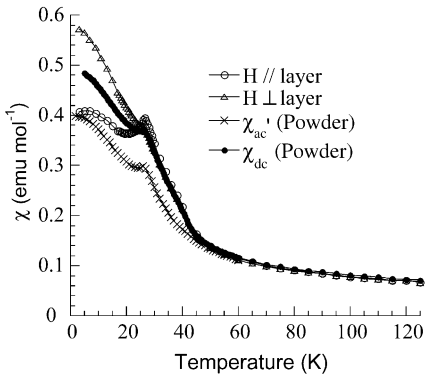

Figure 3. Temperature dependence of the ac (crosses) and dc susceptibilities of a powdered sample (solid circles) and the dc susceptibility of the oriented sample parallel (open circles) and perpendicular (open triangles) to the *bc* plane.

a feature that is consistent with the absence of spontaneous magnetization and magnetic hysteresis. Therefore, these features indicate a system that possibly consists of fully compensated moments. However, for an antiferromagnetic sample one would expect a decrease in the susceptibility of a randomly oriented sample below the Néel transition to a minimum value of 2/3 that at the maximum.[18] This is not the case here since, after a maximum at the transition, χ increases again below T_N, as shown in Figures 2 and 3. The isothermal magnetization of the polycrystalline sample at 2 K (not shown) displays a featureless increase with increasing field without any hysteresis. To more fully elucidate this peculiar magnetic ground state of the compound, we performed dc susceptibility measurements on some selected crystals with well-defined morphology, embedded in poly(methyl methacrylate), which was cast from dichloromethane solution in a flat-bottomed plastic beaker. As the crystals are platelets they settled with preferential alignment of the plate surface (crystallographic *bc* plane) parallel to the faces of the polymer disc. This allowed measurements of the magnetic anisotropy of the system with the applied magnetic field perpendicular or parallel to the *bc* plane. As shown in the Figure 3, the transition is much better defined for a field parallel to the surface of the platelets. Moreover, at lower temperature, the susceptibility reaches a plateau, whereas for the other orientation it continuously increases. The curve for the powder sample is an average of those of the two orientations. We also note that χ' has similar temperature dependence but is slightly smaller than χ_{dc} below 50 K. The isothermal magnetization of the aligned sample at 2 K (Figure 4) shows a featureless increase for the applied field perpendicular to the surface, while it exhibits a kink at 15 kOe for the parallel orientation. No hysteresis was observed in the two cases, and the magnetization at the highest field (50 kOe) was only 4.2 μ_B as opposed to the expected

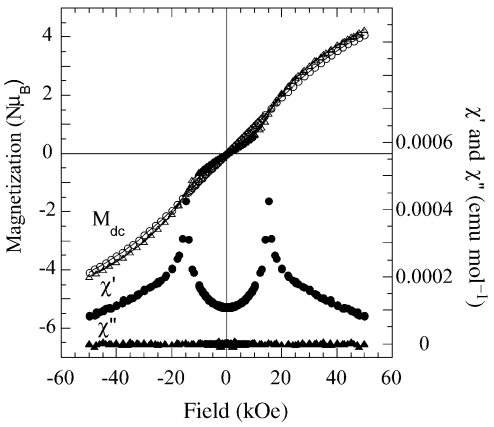

Figure 4. Isothermal magnetization at 2 K for a field applied parallel (triangles) and perpendicular (circles) to the *bc* plane. Field dependence of ac susceptibilities (solid circles and triangles) for a field parallel to the *bc* plane.

15 μ_B if all moments were parallel to the field. To better define the change in slope, we performed a pseudo-mutual-inductance experiment using the same SQUID apparatus by measuring the ac susceptibility for each applied field of the isothermal dc magnetization measurements. As there is no magnetic loss the superposed ac susceptibilities have no frequency dependence, and we therefore measure the slope at each field. As expected, the result is a sharp peak only in the field dependence of the real component at 15 kOe (Figure 4). This anomaly is associated with the spin flop of antiferromagnets.[19] Again, no hysteresis is present.

Specific heat study: The specific heat as a function of temperature (Figure 5) shows two anomalies. The first is the sharp λ anomaly at 26 K confirming the presence of long-range magnetic transition, in good agreement with the mag-

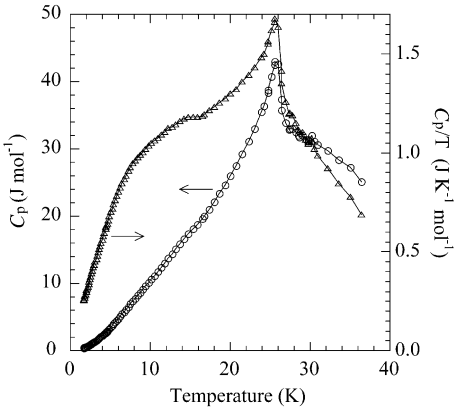

Figure 5. Temperature dependence of the heat capacity C_p, corrected for the lattice contribution and after normalization with temperature (C_p/T).

netic measurements. The second is the broad hump below 26 K that suggests possible low-dimensional effects or short-range magnetic ordering. The latter is more pronounced when C_p/T is plotted versus T.[20] Integration of the data indicates that a large fraction of the entropy is due to short-range ordering.

Magnetic structure: The magnetic structure was solved from neutron powder-diffraction data collected at 13 temperatures ranging between 1.4 and 35 K. A comparison of the data recorded at the temperature extremes (Figure 6) reveals the appearance of intense new Bragg reflections at 1.4 K. Two kinds of new sharp Bragg peaks are evident: enhanced existing nuclear Bragg peaks and new diffraction peaks. The latter correspond to peaks indexed with the same unit-cell parameters but normally systematically absent in the nuclear space-group symmetry, that is, $h0l$ peaks with odd l. This means that the magnetic unit cell is identical to the nuclear unit cell and corresponds to a propagation vector $\boldsymbol{k}=(0, 0, 0)$. Numerous individual magnetic peaks are indeed observed with fairly high intensities. In addition, an increase in the background is clearly evident and gives rise to a broad hump with a maximum around $2\theta=30°$ that is visually clearer for the 35 K data. Its intensity appears to reach a maximum close to the magnetic transition temperature of 26 K. However, as confirmed by the following refinements, it is still present at 1.4 K. Moreover, other, less visible humps are also present. Data collected during sample cooling reveal that the background is flat between 120 and 200 K. The major hump starts to appear at around 100 K and becomes very clear at around 65 K. Both effects, new Bragg reflections and broad humps, appear to be magnetic in origin and have been related to magnetic long-range ordering (LRO) and short-range ordering (SRO), respectively.

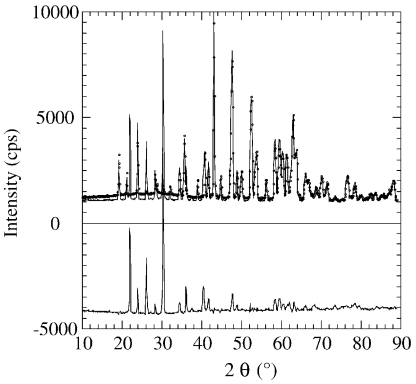

Figure 6. Neutron diffraction data at 1.4 (line) and 35 K (circles) and their difference (bottom line, offset by 4000 cps) showing the sharp magnetic Bragg peaks due to LRO and the broad hump due to SRO.

Let us first consider the magnetic structure determination of the LRO. A comparison of the difference between data collected above and below T_N for the Ni and Mn analogues reveals that the magnetic structures are quite different.[12a] Consequently, another model was sought for the Mn compound. We first performed a magnetic group theory calculation by applying Bertaut's representation-analysis method to the *Pbcm* space group,[21] $\boldsymbol{k}=(0, 0, 0)$ propagation vector and 8e [Mn(1)] and 4d [Mn(2)] Wyckoff positions, as for the Ni analogue. The eight one-dimensional irreducible representations (IR) are determined,[22a] namely Γ_1 to Γ_8, which are associated with basis vectors (magnetic structures) for both Mn(1) and Mn(2).[22b] Each Γ_i ($i=1$–8) is involved in Mn(1) and Mn(2) "magnetic arrangements", according to:

$$\text{Mn(1) (8e)}: \; 3\Gamma_1+3\Gamma_2+3\Gamma_3+3\Gamma_4+3\Gamma_5+3\Gamma_6+3\Gamma_7+3\Gamma_8$$

$$\text{Mn(2) (4d)}: \; \Gamma_1+2\Gamma_2+\Gamma_3+2\Gamma_4+2\Gamma_5+\Gamma_6+2\Gamma_7+\Gamma_8$$

If solutions involving basis vectors associated with distinct Γ_i are not forbidden, one must first check for basis vectors within each Γ_i. In the present case Γ_6 leads to the best calculated magnetic reliability factor, with the magnetic moments of Mn(2) pointing along the c axis and those of Mn(1) lying in the bc plane (Table 7; the M_x component is not significant).

Table 7. Magnetic arrangements.[a]

Atom	M//***a***	M//***b***	M//***c***
Mn11–Mn18	+−+−+−+−	+−+−−+−+	+−−+−++−
Mn21–Mn24	0	0	+−+−

[a] The Mn1i and Mn2i positions are related by the following relations: Mn11 (x, y, z); Mn12 ($-x$, $-y$, $-z$); Mn13 ($-x$, $-y$, $1/2+z$); Mn14 (x, y, $1/2-z$); Mn15 (x, $1/2-y$, $-z$); Mn16 ($-x$, $1/2+y$, z); Mn17 ($-x$, $1/2+y$, $1/2-z$); Mn18 (x, $1/2-y$, $1/2+z$); Mn21 (x, y, $1/4$); Mn22 ($-x$, $-y$, $3/4$); Mn23 ($-x$, $1/2+y$, $1/4$); Mn24 (x, $1/2-y$, $3/4$).

Note that Γ_6 is associated with the magnetic arrangement given above, for which, for instance, the sequence +−+−+−+− holds for the components of the magnetic moments of Mn11 to Mn18 atoms along the crystallographic a axis. Within Γ_6, no magnetic moment is allowed along a and b for Mn(2) atoms. All the other models were checked but they do not reproduce the observed intensities of the magnetic diffraction peaks.

Although the intensities of the nuclear and magnetic peaks are satisfactorily calculated, this model does not account for the presence of humps in the background (Figure 6). The humps are more prominent at higher temperatures than at 1.4 K. Their occurrence can be attributed to the presence of magnetic short-range ordering (SRO). Therefore, we introduced a second magnetic phase with the same structure and IR (Γ_6) but with a different coherence length, which was refined. Such an approach supposes that the volume distribution of both phases, LRO and SRO, is homogeneous. The standard deviations of the components of the magnetic moments (M_x of Mn(1) is not significant) are quite high (Table S3, Supporting Information) compared to those of the LRO phase, but the refinement still converges to an acceptable R_{mag} value of 13.6% for this SRO phase (Figure 7).

The next step concerns the evolution of the magnetic structure with temperature, that is, the direction and magni-

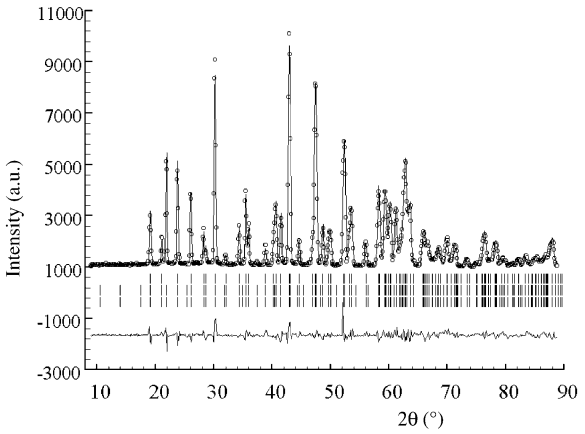

Figure 7. Observed (open circles) and calculated (solid line) profiles of the powder neutron diffraction pattern of $[Mn_3(OD)_2(SO_4)_2(D_2O)_2]$ obtained on the G4.1 diffractometer at 1.4 K with position of the Bragg reflections (short vertical lines, top line for nuclear, middle line for LRO, bottom line for SRO) and difference between observed and calculated profiles.

tudes of the Mn moments. Therefore, the same model was used to refine the parameters from the data collected with increasing temperature between 1.4 and 35 K. The magnetic structure (Γ_6) is observed for all temperatures below T_N for both the long-range and short-range magnetic phases. For the data recorded at $T \geq 27$ K, only the second magnetic phase (SRO) is considered, as the LRO occurs at 26 K (see Table S4, Supporting Information, for data at 35 K). Since the humps are minima at 1.4 K, one expects a better agreement at higher temperatures. This is indeed the case, since the R_{mag} factor for the second magnetic phase continuously decreases from 13.6% at 1.4 K to about 6% at 35 K. Refinements of the data collected at low temperatures yield the thermal variations of the Mn(1) and Mn(2) magnetic moments, as shown in Figure 8.

Concerning the magnetic structure, the first observation is that a model different to that of the nickel compound is found although the moments remain in the *bc* plane in both cases. For the Mn analogue the orientations of the moments

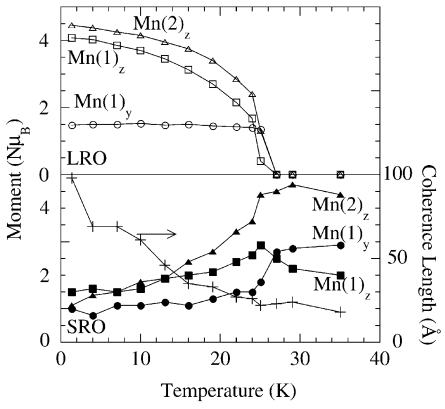

Figure 8. Temperature dependence of the moment components along the principal crystallographic axes for the short-range (full symbols) and long-range (open symbols) magnetic orderings and of the estimated coherence length of the short-range order (+).

are not along any principal crystallographic axis. This explains why different neutron powder diffractograms were observed for the Ni and Mn compounds in the ordered state. For the Ni compound all moments are oriented along the *b* axis. In the case of Mn, the magnetic structure is composed of two components related to the LRO and SRO, as mentioned earlier. In the LRO state, at 1.4 K, the moments of Mn(1) are along a direction making a 20° angle with the *c* axis in the *bc* plane, while those of Mn(2) coincide with the *c* axis (Figure 9). The magnetic moments have similar

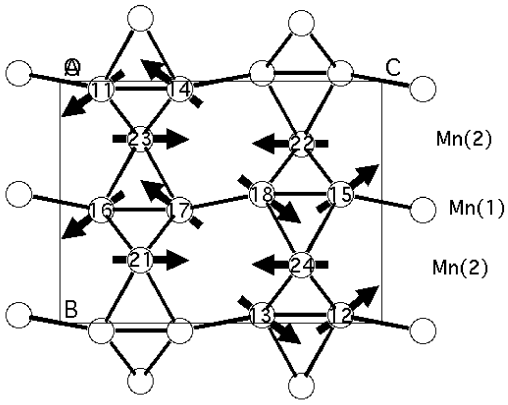

Figure 9. Long-range ordered magnetic structure at 1.4 K. The numbering of the atoms is defined in the text, and the types of atom are indicated on the right.

values of 4.34(7) and 4.44(7) μ_B for Mn(1) and Mn(2), respectively, that is, values approaching the expected 5 μ_B for Mn^{2+}. Note that for Mn(1) the M_z component progressively decreases with increasing temperature, whereas the M_y value is nearly constant in the same temperature range. Consequently, the Mn(1) moment moves towards a direction closer to the *b* axis as the temperature approaches the Néel transition and reaches a value of 74° with respect to the *c* axis at 25 K.

The diffraction data in the SRO state, as evidenced by the observation of humps in the background, were refined with the same model as for the LRO phase, that is, with components M_y and M_z for Mn(1) and only M_z for Mn(2). It results in a good fit of the observed hump, which is much better for higher temperatures at which the signal is more pronounced. For the SRO phase, one observes a continuous increase, within the experimental errors, of all magnetic components, that is, M_y and M_z of Mn(1) and M_z of Mn(2). Concerning the orientation of the magnetic moment of Mn(1), it remains quite constant between 1.4 K and T_N at a value of around 32° with respect to the *c* axis. Above T_N, one observes an increase in M_y [Mn(1)] and a decrease in M_z [Mn(1) and Mn(2)]. At 35 K, the orientation becomes closer to the *b* axis with an angle of 55° with respect to the direction of the *c* axis. Above T_N the data are restricted to three temperatures and some care must be taken with regard to these trends.

Finally, we note that for each Mn ion, the overall moment including both phases and defined as $(M_{SRO}^2 + M_{LRO}^2)^{1/2}$, where M_{SRO} is the magnetic moment of a Mn ion in the

SRO phase and M_{LRO} its equivalent in the LRO phase, is always less than the expected 5 μ_B; the values at 1.4 K are 4.69 and 4.56 μ_B for Mn(1) and Mn(2), respectively. The isotropic coherence length of the SRO phase decreases with increasing temperature from about 95 Å at 1.4 K to about 20 Å near the Néel temperature (Figure 8). Table S5 (Supporting Information) summarises the magnetic-moment components and orientations and the values of the coherence length at different temperatures. The calculated diffraction patterns resulting from the contributions of the nuclear, LRO and SRO structures are plotted on Figure 10 for

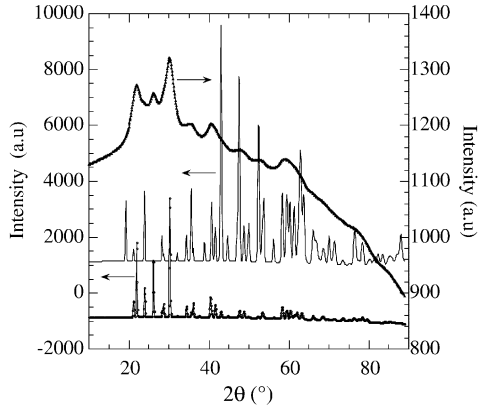

Figure 10. Plot of the calculated diffraction patterns of nuclear (solid line, middle), LRO (line and circles, bottom) and SRO (line and triangles, top) structures obtained by refinement of the experimental data at 16 K. For SRO the *y* scale has been magnified.

the intermediate temperature of 16 K, at which each phase has a comparable contribution. For the SRO phase (its scale is different from the others), the extreme broadening of the diffraction lines clearly results in the formation of the humps.

The short-range magnetic ordering can be considered as a local tendency of the magnetic moments within a trimer to order. The rotation of the moment as a function of temperature may be due to the frustration of the triangular unit and the presence of both ferromagnetic and antiferromagnetic exchange interactions, as expected for the observed Mn-O-Mn angles falling into two ranges below and above 98°,[23] the critical angle for F/AF crossover. It may be regarded as a magnetic gel in which the coherence length increases to as much as 100 Å at 1.4 K. This frustration and gel-like nature may be responsible for 1) the gradual increase in the susceptibilities (ac and dc) below the Néel temperature, 2) the low spin-flop field, 3) the broad hump in the neutron diffraction patterns, and 4) the broad peak in the heat capacity curve. The long-range ordering can then be considered as a coherent organization of the moments of each trimer within the cell and over quite long distances. Here, the ordered state consists of the resultant moments of two trimers pointing along the *c* axis and the other two in the magnetic unit cell pointing in the opposite direction. Further studies such as EPR may shed some light on these anomalous behaviours.

Conclusion

$[Mn_3(OH)_2(SO_4)_2(H_2O)_2]$ and its deuterated analogue were obtained, together with two other crystalline phases, by controlled hydrothermal synthesis and were found to be isostructural with $[Ni_3(OH)_2(SO_4)_2(H_2O)_2]$. It exhibits unusual magnetic behaviors, heat capacity and magnetic structure that were interpreted by the presence of both short-range and long-range magnetic orders below the Néel temperature (26 K). The moment of one of the manganese atoms rotates by 54° within the *bc* plane as a function of temperature below T_N.

Experimental Section

General characterization: Differential thermal (DTA) and thermogravimetric (TGA) analyses were performed in air on a TA-SDT-Q600 apparatus at a heating rate of 3 °C min^{-1}. Infrared spectra were recorded on an ATI Mattson spectrometer by transmission through a KBr pellet containing about 1 % of the compound at a resolution of 4 cm^{-1} and in the range 500–4000 cm^{-1}. Powder X-ray diffraction patterns were recorded on a D500 Siemens diffractometer ($Cu_{K\alpha}$ radiation, $\lambda = 1.5418$ Å) equipped with a back-monochromator to reduce the fluorescence due to manganese.

Synthesis: Commercial-grade chemicals were used for all synthetic procedures, and water was distilled before use. $[Mn_3(OH)_2(SO_4)_2(H_2O)_2]$ was prepared by hydrothermal treatment of an aqueous suspension (30 mL), obtained by mixing solutions of manganese(II) sulfate $Mn(SO_4)\cdot H_2O$ (4 g, 23.7 mmol) and sodium hydroxide (0.38 g, 9.5 mmol), that is, in an Mn:Na molar ratio of 5:2, at 200 °C for three days under autogenous pressure in 125-mL autoclaves. The autoclaves were then quenched in cold water, and the solid product was separated from the mother liquor by sedimentation and decantation, washed several times with distilled water to remove soluble salts, and then with ethanol and acetone and finally dried in air. The title compound was obtained as beige rectangular flat plates for all investigated Mn:Na ratios between 10:3 and 10:5 and for fixed temperatures of 170, 200 and 240 °C. Two other minor phases were occasionally observed. One of them, $Mn_2(OH)_2SO_4$, having the habit of pink prismatic blocks, was identified by single-crystal X-ray diffraction. Its magnetic behavior is characterized by a canted antiferromagnetic state below 42 K and it displays no hysteresis in the isothermal magnetization at 2 K. The other phase, which formed as fine colourless needles, has not been structurally characterized, though XRPD indicates a possible layered structure with an interlayer distance of 9.67 Å. It is a magnet with a Curie temperature of 21 K. The use of a Mn/Na ratio of 5/2 and a reaction temperature of 200 °C were found to be the optimum conditions to minimize the quantity of the other two phases.

Samples for neutron powder diffraction were prepared under the optimised conditions by replacing water (H_2O) by heavy water (D_2O). Using D_2O reduce the effect of the high incoherent scattering factor of hydrogen, which gives rise to an increase in the background that can disturb further analysis. This sample fortunately showed no peaks within the detection limits of the instruments corresponding to the other two phases in its X-ray and neutron diffraction patterns. IR spectra and final refinement of the neutron diffraction data revealed that D for H substitution was achieved in good yield.

X-ray crystallography and nuclear structure refinement: Single-crystal X-ray data were collected at room temperature on a selected crystal mounted on a glass fiber. A single set of 180 frames (each frame measured twice), 20 s/frame, ϕ scan of 1°/frame, crystal detector distance of 30 mm, $\theta = 0°$, $\kappa = 0°$ was collected on a Nonius Kappa CCD diffractometer at the Service Commun de Rayons X, Université Louis Pasteur, Strasbourg. Structure refinement, starting from the atomic positions of the corresponding nickel compound,[12a] was performed with SHELXL-93.[24] The final refinement included anisotropic displacement parameters and the empirical extinction correction within SHELXL-93, which includes ab-

normal absorption and mosaicity extinction. The atomic coordinates of hydrogen atoms were located in the difference Fourier maps and were not refined. Additional experimental details are given in Table 2 and in the Supporting Information. Table 3 lists the fractional atomic coordinates, and Table 4 gives the bond lengths and angles from X-ray refinement. For convenience, the oxygen atoms of the sulfate group, of the hydroxyl groups and of the water molecule are labelled O, OH and OW, respectively. For H [D for neutron data] atoms, H(1) [D(1)] and H(2) [D(2)] correspond to OH(1) [OD(1)] and OH(2)[OD(2)] groups, respectively, whereas HW [DW] refers to the H [D] atoms of the water molecule. Further details on the crystal structure investigations may be obtained from the Fachinformationszentrum Karlsruhe, 76344 Eggenstein-Leopoldshafen, Germany (fax: (+49) 7247-808-666; e-mail: crysdata@fiz-karlsruhe.de), on quoting the depository number CSD-413409.

The neutron diffraction experiments were performed at the Laboratoire Léon Brillouin (CEA, Saclay) using the G4.1 and G4.2 diffractometers. The multidetector (800 cells) G4.1 powder diffractometer ($\lambda = 2.4266$ Å) was used for the determination of the magnetic structure and the study of the temperature dependence of the magnetic structure in the ordered state. 13 diffraction patterns were recorded in the range $2\theta = 10$–$89.9°$ at different fixed temperatures between 1.4 and 35 K. The powder sample was held in a cylindrical vanadium can and held in a helium cryostat. The room-temperature structure refinement was performed from data collected on the same sample by using the high-resolution G4.2 diffractometer ($\lambda = 2.3433$ Å). Nuclear and magnetic structures were refined using the FULLPROF suite of programs.[25] The nuclear scattering lengths ($b_{Mn} = -0.3730 \times 10^{-12}$, $b_S = 0.2847 \times 10^{-12}$, $b_O = 0.5803 \times 10^{-12}$, $b_D = 0.6671 \times 10^{-12}$ and $b_H = -0.3739 \times 10^{-12}$ cm) and magnetic form factors for manganese were those included in the program.

Magnetization and specific heat measurements: Following numerous frustrating failures with multiphase samples, the magnetic susceptibility measurements were finally performed on crystals of well-defined morphology, which were selected under an optical microscope and washed carefully with ethanol. Data were collected while cooling from 300 to 2 K in an applied field of 100 Oe by means of a Quantum Design MPMS-XL magnetometer. Isothermal magnetization was measured at 2 K in field spanning ±50 kOe. Ac magnetization measurements were performed with the same apparatus in zero dc field and an alternating field of 1 Oe oscillating at 17 Hz. Specific-heat measurements between 1.7 and 38 K were carried out in zero field using a home-built equipment and employing a quasi-adiabatic method. Several samples were measured in both magnetization and heat-capacity experiments to check the reproducibility.

Acknowledgement

This work was supported by the CNRS and CEA (France). We thank C. Heckmann, J.-P. Lambour, A. Decian, and A. Derory for technical assistance and A. Kurbakov for the measurements of room-temperature neutron powder data on G4.2. M.B.S. thanks the ′Ministère de L′Enseignement Supérieur de Tunisie′ for a start-up thesis grant.

[1] S. Feng, R. Xu, *Acc. Chem. Res.* **2001**, *34*, 239–247.
[2] M. Kurmoo, *Mol. Cryst. Liq. Cryst.* **2002**, *379*, 271–278.
[3] A. Rabenau, *Angew. Chem.* **1985**, *97*, 1017–1032; *Angew. Chem. Int. Ed. Engl.* **1985**, *24*, 1026–1040.
[4] a) G. Ferey, *Chem. Mater.* **2001**, *13*, 3084–3098; b) N. L. Rosi, J. Eckert, M. Eddaoudi, D. Vodak, J. Kim, M. O'Keefe, O. M. Yaghi, *Science* **2003**, *300*, 1127–1130; c) K. Kim, *Chem. Soc. Rev.* **2002**, *31*, 96–107.
[5] a) H. Kumagai, C. J. Kepert, M. Kurmoo, *Inorg. Chem.* **2002**, *41*, 3410–3422; b) M. Kurmoo, H. Kumagai, M. A. Green, B. W. Lovett, S. J. Blundell, A. Ardavan, J. Singleton, *J. Solid State Chem.* **2001**, *159*, 343–351.
[6] a) T. Maschmeyer, F. Rey, G. Sankar, J. M. Thomas, *Nature* **1995**, *378*, 159–162; b) C. N. R. Rao, S. Natarajan, A. Choudhury, S. Neeraj, A. A. Ayi, *Acc. Chem. Res.* **2000**, *33*, 80–87; c) P. M. Forster, A. K. Cheetham, *Angew. Chem.* **2002**, *114*, 475–477; *Angew. Chem. Int. Ed.* **2002**, *41*, 457–459; d) A. K. Cheetham, G. Ferey, T. Loiseau, *Angew. Chem.* **1999**, *111*, 3460–3462; *Angew. Chem. Int. Ed.* **1999**, *38*, 3268–3270; e) H. Li, M. Eddaoudi, M. O'Keeffe, O. M. Yaghi, *Nature* **1999**, *402*, 276–279; f) J. Kim, B. Chen, T. M. Reineke, H. Li, M. Eddaoudi, D. B. Moler, M. O'Keeffe, O. M. Yaghi, *J. Am. Chem. Soc.* **2001**, *123*, 8239–8247; g) M. O'Keeffe, M. Eddaoudi, H. Li, T. Reineke, O. M. Yaghi, *J. Solid State Chem.* **2000**, *152*, 3–20.
[7] a) R. K. Eby, F. C. Hawthorne, *Acta Crystallogr.* **1993**, *49*, 28–56; b) F. C. Hawthorne, L. A. Groat, R. K. Eby, *Can. Mineral.* **1989**, *27*, 205–209.
[8] Special issue on "New Horizons for Magnetic Solids Based on molecules: From High-T_C magnets to Nanomagnets to Devices" (Ed.: K. R. Dunbar), *J. Solid State Chem.* **2001**, *159*
[9] a) S. A. Solin, *Annu. Rev. Mater. Sci.* **1997**, *27*, 89–115; b) V. Mitchell, *Pillared Layered Structures: Current trends and applications*, Elsevier, London **1990**; c) *Inorganic Materials* (Eds.: D. O'Hare, D. W. Bruce), Wiley, Chichester, **1992**; d) J. M. Thomas, *Philos. Trans. R. Soc. London Ser. A* **1990**, *333*, 173–207.
[10] a) M. Richard-Plouet, S. Vilminot, M. Guillot, M. Kurmoo, *Chem. Mater.* **2002**, *14*, 3829–3836; b) M. Richard-Plouet, S. Vilminot, *Solid State Sci.* **1999**, *1*, 381–393; c) M. Richard-Plouet, S. Vilminot, *J. Mater. Chem.* **1998**, *8*, 131–137; d) M. Guillot, M. Richard-Plouet, S. Vilminot, *J. Mater. Chem.* **2002**, *12*, 851–857.
[11] a) A. Rujiwatra, C. J. Kepert, J. B. Claridge, M. J. Rosseinsky, H. Kumagai, M. Kurmoo, *J. Am. Chem. Soc.* **2001**, *123*, 10584–10594; b) A. S. Wills, *Phys. Rev. B* **2001**, *63*, 064430; c) A. S. Wills, A. Harrison, C. Ritter, R. I. Smith, *Phys. Rev. B* **2000**, *61*, 6156–6169; d) D. Papoutsakis, D. Grohol, D. G. Nocera, *J. Am. Chem. Soc.* **2002**, *124*, 2647–2656.
[12] a) S. Vilminot, M. Richard-Plouet, G. André, D. Swierczynski, F. Bourée-Vigneron, M. Kurmoo, *Inorg. Chem.* **2003**, *42*, 6859–6867; b) S. Vilminot, M. Richard-Plouet, G. André, D. Swierczynski, M. Guillot, F. Bourée-Vigneron, M. Drillon, *J. Solid State Chem.* **2003**, *170*, 255–264; c) S. Vilminot, M. Richard-Plouet, G. André, D. Swierczynski, F. Bourée-Vigneron, E. Marino, M. Guillot, *Cryst. Eng.* **2002**, *5*, 177–186.
[13] F. A. Cotton, G. Wilkinson, *Advanced Inorganic Chemistry*, 5th Ed., Wiley, New-York, **1988**, p. 697.
[14] C. S. G. Phillips, R. J. P. Williams, *Inorganic Chemistry*, Oxford University Press, Oxford, **1965**, p. 151.
[15] M. Evain, U-FIT: A cell parameter refinement program, I.M.N., Nantes, France, **1992**
[16] W. Mikenda, *J. Mol. Struct.* **1986**, *147*, 1–15.
[17] I. D. Brown, D. Altermatt, *Acta. Cryst. B* **1985**, *41*, 244–247.
[18] a) R. L. Carlin, *Magnetochemistry*, Springer-Verlag, Berlin, **1986**; b) O. Kahn, *Molecular Magnetism*, VCH, New-York, **1993**.
[19] L. J. De Jongh, A. R. Miedema, *Adv. Phys.* **2000**, *49*, 947–1170.
[20] *Magnetic Properties of Layered Transition Metal Compounds*, (Ed.: L. J. De Jongh), Kluwer Academic Publishers, Dordrecht, **1990**.
[21] E. F. Bertaut, *Acta Crystallogr.* **1968**, *24*, 217.
[22] a) KAREP—a program for calculating irreducible space group representations E. Hovestreydt, I. Aroyo, S. Sattler, H. Wondratschek, *J. Appl. Crystallogr.* **1992**, *25*, 544; b) BASIREPS—a program for calculating non-normalized basis functions of the irreducible representations of the little group Gk for atom properties in a crystal, J. Rodriguez-Carvajal, Laboratoire Léon Brillouin (CEA-CNRS), CEA Saclay, Gif sur Yvette, France.
[23] a) J. B. Goodenough, *Magnetism and the Chemical Bond*, Wiley, New York, **1963**; b) J. Kanamori, *J. Phys. Chem. Solids* **1959**, *10*, 87; c) J. Kanamori in *Magnetism, Vol. I* (Eds.: G. T. Rado, H. Suhl), Academic Press, New York, **1963**, p. 127; A. Herpin, *Théorie du Magnétisme*; Presse Universitaire de France, Paris, **1968**.
[24] G. M. Sheldrick, SHELXL-93, Program for the refinement of crystal structures, University of Göttingen, Germany, **1993**.
[25] J. Rodriguez-Carvajal, FULLPROF: Rietveld, profile matching and integrated intensity refinement of X-ray and/or neutron data, 3.5d version (**1998**), Léon-Brillouin Laboratory, CEA Saclay, France.

Received: October 21, 2003
Revised: December 19, 2003 [F5645]

